

Correcting STIS CCD Photometry for CTE Loss¹

Paul Goudfrooij

Space Telescope Science Institute, Baltimore, MD 21218, USA

Randy A. Kimble

NASA Goddard Space Flight Center, Code 681, Greenbelt, MD 20771, USA

Abstract. We review the various on-orbit imaging and spectroscopic observations that are being used to characterize the Charge Transfer Efficiency (CTE) of the Charge-Coupled Device (CCD) of the Space Telescope Imaging Spectrograph (STIS) aboard the *Hubble Space Telescope*. We parametrize the CTE-related loss for aperture photometry of point sources in terms of dependencies on X and Y positions, the brightness of the source, the background level, and the time of observation. Our parametrization of the CTE loss is able to correct point source photometry with STIS to an accuracy similar to the Poisson noise associated with the source detection itself.

1. Introduction

Astronomical observation was revolutionized more than two decades ago by charge-coupled device (CCD) technology, due to a combination of generally linear response over a very large dynamic range and high quantum efficiency. One shortcoming of CCDs, however, is the imperfect transfer of charge from one pixel to the next. Charge Transfer Efficiency (CTE) is the term commonly used to describe such charge loss, and it is quantified by the fraction of charge successfully moved (clocked) between adjacent pixels. In practice it is often more useful to use the term Charge Transfer *Inefficiency* ($CTI = 1 - CTE$). The observational effect of CTI is that a star whose induced charge has to traverse many pixels before being read out appears to be fainter than the same star observed near the read-out amplifier.

Laboratory tests have shown that CTE loss of CCDs increases significantly when being subjected to radiation damage (e.g., Janesick 1991). This is particularly relevant for spaceborne CCDs such as those aboard *Hubble Space Telescope (HST)*, where the cosmic ray flux is significantly higher than on the ground. The purpose of the current paper is to characterize the CTI of the CCD of the Space Telescope Imaging Spectrograph (STIS) for point source photometry in terms of its dependencies on the X and Y positions, target intensity, background counts, measurement aperture size, and elapsed on-orbit time. Earlier on-orbit characterizations of the CTI of the STIS CCD have been reported by Gilliland, Goudfrooij, & Kimble (1999) and Kimble, Goudfrooij, & Gilliland (2000). The current paper uses two more years of on-orbit data, which provides a significantly more accurate temporal dependence. Furthermore, we provide (for the first time) an algorithm to correct STIS CCD imaging photometry for CTI.

The STIS CCD is a 1024×1024 pixel, backside-illuminated device with $21 \mu\text{m} \times 21 \mu\text{m}$ pixels. It was fabricated by Scientific Imaging Technology (SITE) with a coating process that allows it to cover the 200–1000 nm wavelength range for STIS in a wide variety of

¹Based on observations with the NASA/ESA *Hubble Space Telescope*, obtained at the Space Telescope Science Institute, which is operated by AURA, Inc., under NASA contract NAS5-26555.

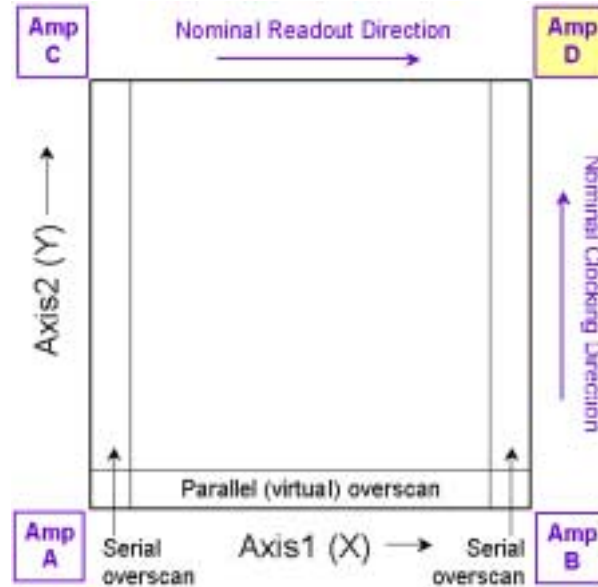


Figure 1. Schematic architecture of the STIS CCD. The 1024×1024 pixel device has two serial registers and four readout amplifiers. The nominal amplifier (amp D) is at the top right.

imaging and spectroscopic modes. Key features of the STIS CCD architecture are shown schematically in Figure 1. Two serial registers are available. A read-out amplifier is located at all four corners, each with an independent analog signal processing chain. The full image can be read out through any one of the four amplifiers, or through two- and four-amplifier combinations. By default, science exposures employ full-frame readout through amplifier ‘D’, which features the lowest read-out noise. Further technical details regarding the STIS CCD in particular is provided in Kimble et al. (1994), while background information on the design of STIS in general can be found in Woodgate et al. (1998).

This paper is organized as follows. We first address CTE degradation. Section 2 describes methods used to monitor the CTI: One method using standard, internal dark exposures, and two methods designed to quantify the CTI appropriately to observations of point sources in sparse fields for spectroscopic and imaging modes. We derive functional dependences of the CTI on source and background counts, X and Y position on the CCD, and elapsed on-orbit time in Section 3. Finally, Section 4 summarizes these results and describes an upcoming method to apply the CTI correction to photometric data tables derived from STIS images.

2. Monitoring the CTE

2.1. Cosmic Ray Tails

An elegant method of monitoring CTI using the average profiles of cosmic rays observed in standard dark current measurements (and hence not requiring any valuable pointed, “external” telescope time) has been developed by Riess, Biretta, & Casertano (1999; see also Riess, this volume, p. 47). The method works as follows. While cosmic rays typically produce charge in more than one pixel, their induced charge distribution should *statistically* (i.e., averaged over the whole CCD) be symmetric about their highest-count pixel, without any preferred angular orientation. Hence, any systematic asymmetry in the cosmic ray profiles in the clocking direction of the CCD is a measure of the CTI (through charge

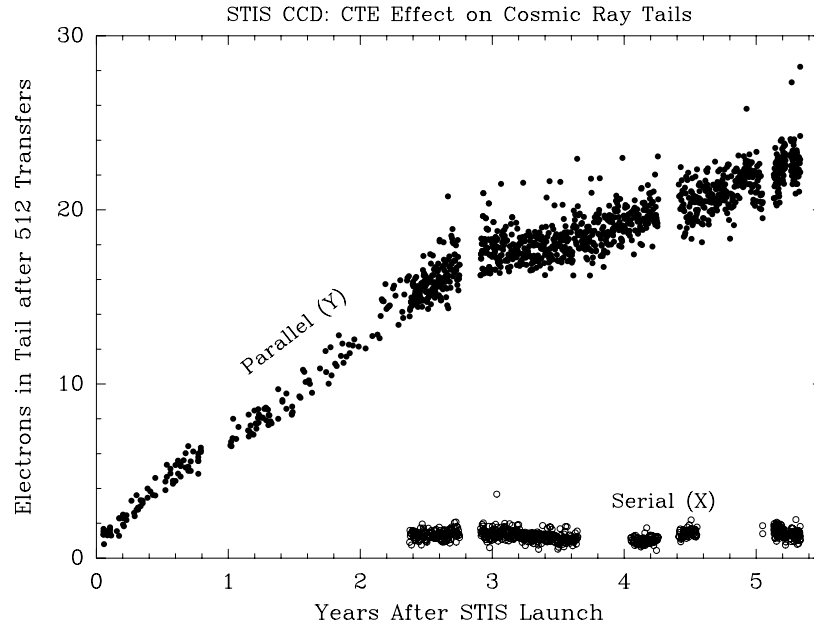


Figure 2. CTI increase with on-orbit time, as measured by the excess signal in the trailing vs. the leading pixels of cosmic ray events detected in standard dark frames. Plotted is the amplitude of that excess signal after 512 transfers (representative for the center of the CCD). Note the *much* stronger CTI in the parallel clocking direction vs. the serial one. The gaps in time indicate extended periods during which STIS was in safe mode (zero-gyro mode and Servicing Mission 3A around 2.8 on-orbit years; Side-1 failure around 4.3 years; Servicing Mission 3B near 5 years). Data on serial CTI are only plotted when the fit was converging.

trapping and subsequent release). Referenced to the highest-count pixel of the cosmic ray event, one measures the excess signal in the trailing pixels relative to that in the leading pixels. Averaging the results over thousands of cosmic rays in dark frames, a significant trailing charge excess is found which grows linearly with distance from the readout amplifier, a clear signature of CTI origin. Figure 2 shows the growth of the cosmic ray tails with on-orbit time, showing (i) the steady growth of the parallel CTI since STIS was placed into *HST*, and (ii) the serial CTI.

Since dark frames are taken daily with the STIS CCD, this method is excellent for providing a finely time-sampled measure of one aspect of CTE performance. However, it does not provide an adequate measure of the dependence of CTI on signal level, and only charge lost beyond a short tail is being measured. Charge trapping with longer time constants is measured using methods described below, which provide measures that are directly applicable to typical imaging and spectroscopic observations with the STIS CCD.

2.2. Internal Sparse Field Test

A novel test method, which we designate the “internal sparse field” test, was developed by the STIS Instrument Definition Team for both ground calibration and in-flight use. It quantifies two key aspects of CTE effects on spectroscopic measurements: (i) The amount of charge lost *outside* a standard extraction aperture, and (ii) the amount of centroid shift experienced by the charge that remains *within* that extraction aperture.

The test utilizes the ability of the STIS CCD and its associated electronics to read out the image with any amplifier, i.e., by clocking the accumulated charge in either direction for both parallel and serial directions. A sequence of nominally identical exposures is taken,

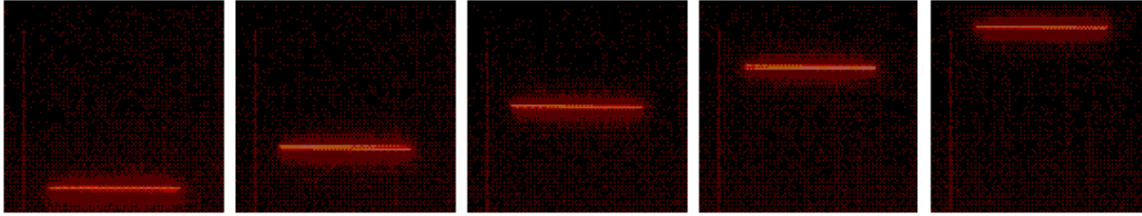


Figure 3. Representative images used for the parallel version of the “internal sparse field” CTE test. At each of the five positions along the CCD columns, a sequence of exposures is taken, alternating between amplifiers ‘D’ and ‘B’. Systematic variation of the relative intensities observed by the two amplifiers as a function of position reveals the CTE effect.

alternating the readout between amplifiers on either side of the CCD (e.g., amps ‘B’ and ‘D’ for measuring parallel CTI). After correcting for (small) gain differences in the two readout amplifier chains, the observed ratio of the fluxes measured by the two amps can be fit to a simple CTE model of constant fractional charge loss per pixel transfer. By inspecting the dependence of the observed flux ratio (e.g., ‘amp B’/‘amp D’) on the source position on the CCD, it can be confirmed that what is measured is indeed consistent with being due to a charge transfer effect.

A key virtue of this method is that neither a correction for flat-field response non-uniformity is required, nor an a-priori knowledge of the source flux (as long as the input source is stable during the alternating exposures). It should be noted that what is being measured is actually a sum of the charge transfer inefficiencies for the two different clocking directions. However, given the identical clocking voltages and waveforms and with the expected symmetry of the radiation damage effects, we believe the assumption that the CTI is equal in the two different directions is a reasonable one.

The implementation of this “internal”¹ version of the sparse field test is as follows. Using an onboard tungsten lamp, the image of a narrow slit is projected at five positions along the CCD columns. At each position, a sequence of exposures is taken, alternating between the ‘B’ and ‘D’ amplifiers for readout. An illustration of such an exposure sequence is depicted in Figure 3. For each exposure, the average flux per column within a 7-row extraction aperture (which is the default extraction size for long slit STIS spectra of point sources, cf. Leitherer & Bohlin 1997) as well as the centroid of the image profile within those 7 rows are calculated. The alternating exposure sequence allows one to separate CTE effects from flux variations produced by warmup of the tungsten lamp. As the slit image extends across hundreds of columns, high statistical precision on CTE performance can be obtained even at low signal levels per column.

Although these data are taken in undispersed (imaging) mode, the illumination is representative for typical spectroscopic observations (as the dispersion direction of STIS CCD spectral modes is along rows). The slit image has a narrow profile (2-pixel FWHM), similar to a point source spectrum. The CTI resulting from this test is “worst-case,” since there is essentially no background intensity (“sky”) to provide filling of charge traps in the CCD array. Early results from this test were reported in Kimble et al. (2000); a comprehensive update will be forthcoming (Goudfrooij et al. 2003, in preparation).

¹“Internal” in this context means that the necessary observations can be performed during Earth occultations, hence not requiring any valuable “external” *HST* observing time.

2.3. External Sparse Field Test

Similar sparse-field CTE tests using “external” astronomical data have also been carried out in flight, on an annual basis (since 1999). These calibration programs (*HST* Program ID’s to date have been 8415, 8854, and 8911) has utilized both imaging and spectroscopy modes. The two observing modes are discussed separately below.

Imaging Test Series of imaging data have been acquired once a year (since 1999) on a sparse field in the outskirts of the Galactic globular cluster NGC 6752, a field containing several hundred stars spanning a large range of intrinsic brightness. Every visit of the field consisted of 3 *HST* orbits, in which several exposures were taken using two different exposure times (20 s and 100 s per exposure). Several repeat exposures were taken at both exposure times, alternating again between opposing readout amplifiers.

The image field is “sparse” in the sense that there are not many stars per CCD row or column. We deliberately choose a portion of NGC 6752 to ensure this, as it is well known that the CTE-induced loss in crowded fields are significantly ameliorated (due to trap filling) relative to the effects on isolated point sources, while the latter is what we intend to measure here. To allow an assessment of the effect of a varying sky background level, we took the data in the so-called Continuously Visible Zone (CVZ) of *HST*, in which the bright Earth comes closer than usual to the telescope pointing direction. The varying amount of scattered light from the bright Earth allows one to obtain a varying “sky” background during the CVZ orbits, and hence to obtain CTI measurements at a suitable range of sky background levels.

Spectroscopy Test Series of spectroscopic data have also been acquired once a year since 1999, as part of the same calibration proposals as the aforementioned imaging CTE tests. The exposure setup is very similar to that used for the imaging exposures mentioned in the previous section (3 orbits per *HST* visit, cycling through three exposure times, alternating between the two different amplifiers). Slitless spectroscopy is performed of a sparse field within NGC 346, a young star cluster in in the Small Magellanic Cloud, again located within the CVZ. The G430L grating is used, which covers the wavelength region 2900–5700 Å at a dispersion of 2.73 Å/pixel.

The sky background of this field features an ionized gas cloud (H II region). Due to the spectral energy distribution of H II regions within the wavelength coverage of the G430L grating (e.g., the three strong emission lines [O II] λ 3727, H β λ 4861 and [O III] λ 5007), the “sky” background spectrum of these (slitless) data features three relatively constant flux levels along the dispersion direction. This aspect of this dataset allows one to average the star spectra over a suitably large number of columns, and hence increase the S/N ratio of the measurements, while the sky background (and hence its charge trap-filling effect) stays relatively constant. Results on the CTI in spectroscopic mode will be presented in Ralph Bohlin’s contribution to this volume (p. 115) as well as in Goudfrooij et al. (2003). We concentrate on the imaging results in the remainder of this paper.

3. CTI Analysis for Aperture Photometry of Point Sources

The images were first sorted into groups with a given exposure time and background level. Images in each group were then averaged together into cosmic-ray-rejected images, using tasks BASIC2D and OCRREJECT in the STIS package of STSDAS. Aperture photometry was then performed using the DAOPHOT-II package (Stetson 1987) as implemented within IRAF using fixed-size apertures.

Representative results on the parallel CTI for a short-exposure imaging dataset acquired in 1999 are shown in Figure 4 in which the observed flux ratio (amp D/amp B) vs. distance from amp B is plotted for two different ranges of stellar flux level per exposure.

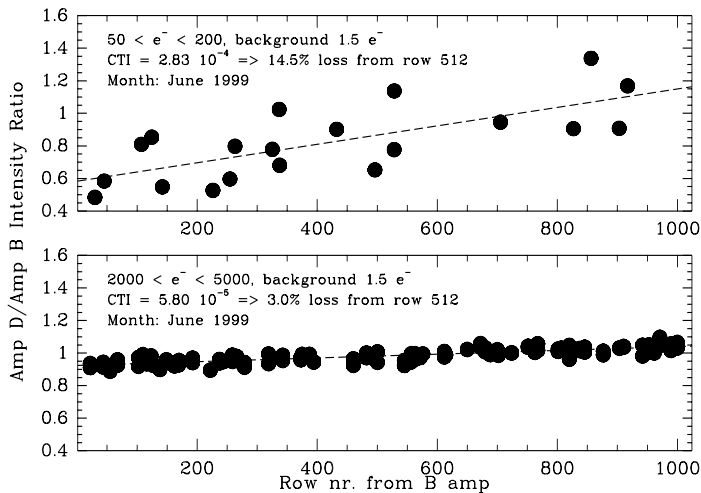


Figure 4. Relative fluxes as a function of position on the CCD, measured by amplifiers ‘D’ and ‘B’ for an image acquired in the external sparse field test. The best-fitting line in each panel has a slope equal to $2 \times \text{CTI}$. Object flux ranges, sky background value, aperture size and fitted CTI values (per pixel) are shown in each panel.

The expected CTE behavior is clearly seen, with the closer readout amplifier systematically measuring a higher stellar flux than the more distant amplifier. In the CTE model we have been considering (i.e., a constant fractional charge loss per pixel transfer), the predicted flux ratio is a straight line with a slope equal to $2 \times \text{CTI}$. It is clear that the CTI decreases with increasing signal level. Note also that the charge loss incurred for parallel clocking through the image area of the CCD is quite substantial for signal levels of a few hundred electrons or less. *Serial* CTIs were also determined, and found to be negligible for all purposes (i.e., orders of magnitude smaller, and consistent with zero given the uncertainties). In what follows, CTI is equated to *parallel* CTI. The default $\text{GAIN} = 1$ setting (i.e., $1.0 \text{ e}^-/\text{ADU}$) is used throughout.

To evaluate the dependence of the measured CTI on aperture size, measurements were made through three popular aperture sizes (diameters of 5, 7, and 11 pixels). The result is depicted in Figure 5. Fortunately, we don’t find any significant difference in CTI among the three apertures used. i.e., one can perform small-aperture photometry (with its increased S/N relative to larger apertures) without incurring a larger CTI.

The dependence of CTI on the sky background, as derived from the 1999 visit of the external imaging sparse field test, is depicted in Figure 6. A particularly striking result from these measurements is the marked decrease in the CTI values for data with increasing sky background. Furthermore, the slope of $\log \text{CTI}$ vs. $\log \text{background}$ decreases systematically with increasing signal level. This suggests that the sky background fills traps in the *bottoms* of the potential wells of the CCD, mostly affecting the transfer of *small* charge packets. This substantial benefit of (only modest) sky background is good news for most STIS CCD imaging observations (which typically have longer exposure times than those used for these tests), in the sense that most exposures will not suffer from the large CTI values experienced during the low-background tests reported here.

3.1. Functional Form for CTI

In evaluating a suitable functional form to characterize the CTI of the STIS CCD, we considered the following. First, CTI values measured for a given combination of signal and sky background levels show a time dependence that is consistent with linear (see

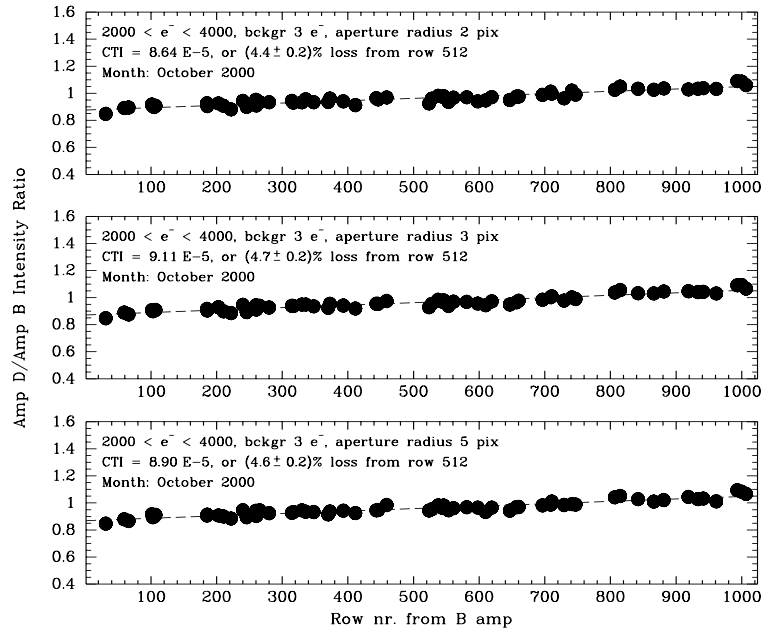


Figure 5. Similar to Figure 4, but the three panels now show results for three different aperture radii at fixed signal level and background. Note that the measured CTI is the same for each aperture (within the errors).

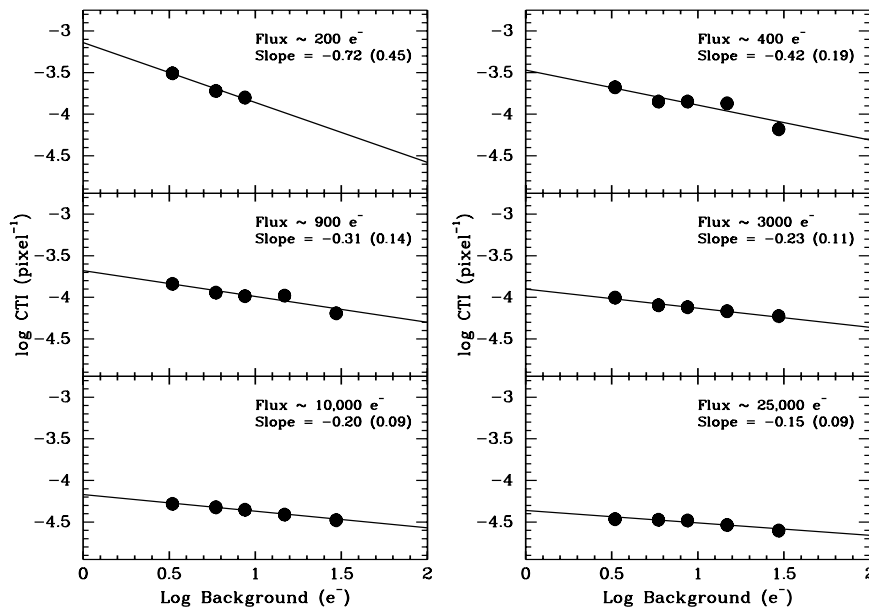


Figure 6. Log CTI as a function of log background for six different flux levels (in October 1999). The flux levels, the slopes of the best-fitting line, and the latter's uncertainties (in parentheses) are mentioned in each panel. Note the systematic decrease of the CTI dependence on the sky background with increasing signal level.

http://www.stsci.edu/hst/stis/proposing/phase2/cy11_update.pdf), as was found earlier for WFPC2 data (Whitmore et al. 1999; Dolphin 2000). Furthermore, a glance at panel (a) of Figure 7 demonstrates that the logarithm of CTI scales roughly linearly with the logarithm of signal level (for a given background level), i.e., $\text{CTI} \propto \exp(-a \ln(\text{counts}))$, while Figure 6 suggests a functional form similar to $\text{CTI} \propto \exp(-a [\text{sky}/\text{counts}]^b)$. We attempted to fit the CTI values with a combination of those two functional forms as well as other (additional) terms. After extensive experimentation, the following functional form produced the best fits to the data:

$$\text{CTI} = (1 + a \text{ yr}) \times b \exp(-c \text{ lcts}) \times \left[d \exp(-e \text{ lbck}) + f \exp\left(-g \left(\frac{\text{bck}}{\text{counts}}\right)^h\right) \right] \quad (1)$$

where

$$\begin{aligned} \text{yr} &\equiv (\text{MJD} - 51831)/365.25 \\ \text{lcts} &\equiv \ln(\text{counts}) - 8.5 \\ \text{bck} &\equiv \text{sqrt}(\text{sky}^2) \\ \text{lbck} &\equiv \ln(\text{sqrt}(\text{sky}^2 + 1)) - 2 \end{aligned}$$

The constants 51831, 8.5, and 2 were roughly the averages of the corresponding parameters in the data, and were included to provide numerical stability as well as to produce independent coefficients (a through h). The $\text{sqrt}(\text{sky}^2)$ term in the “bck” and “lbck” parameters was introduced to avoid logarithms of negative values. The parameter a was determined by defining a set of signal and sky background levels that were in common between the data from all epochs, and measuring the fractional CTI increase per year for all those sets. Parameter a was then defined to be the weighted mean fractional increase of CTI per year (weighted by the inverse variance of the fractional CTI increase for each set). Initial estimates of the values of parameters b through h and their uncertainties were made using bootstrap tests. A robust fit parameter was then minimized using a non-linear minimization routine from *Numerical Recipes* (Press et al. 1992). The resulting best-fit values of the parameters in eq. (1) are listed in Table 1.

Table 1. Best-fit Values of Coefficients in CTI Functional Form

Coeff.	Value	Description
a	0.11 ± 0.03	Time dependence
b	$(9.32 \pm 0.09) 10^{-5}$	CTI normalization
c	0.37 ± 0.01	Flux (count) level dependence
d	0.23 ± 0.02	Normalization for background dependence
e	0.60 ± 0.05	Background level dependence
f	0.48 ± 0.01	Normalization for background/flux ratio dependence
g	1.80 ± 0.10	Background/flux ratio dependence
h	0.40 ± 0.04	Power of background/flux ratio

The quality of this parametrization of the CTI correction is depicted in Figure 7 (panels b–d), separately for each observation epoch. Quantitatively, the CTI parametrization formula yields a correction that is accurate within 7% for any data point. To put this in perspective, an observation of a typical faint object with a signal of 100 e^- and a background of 2 e^- per pixel at the center of the CCD underwent a CTE loss of $\sim 17\%$ in September 2001 (cf. Figure 7d). The CTI parametrization corrects this loss to a photometric accuracy of 1.2%, *which is similar to the uncertainty due to Poisson noise for that object.*

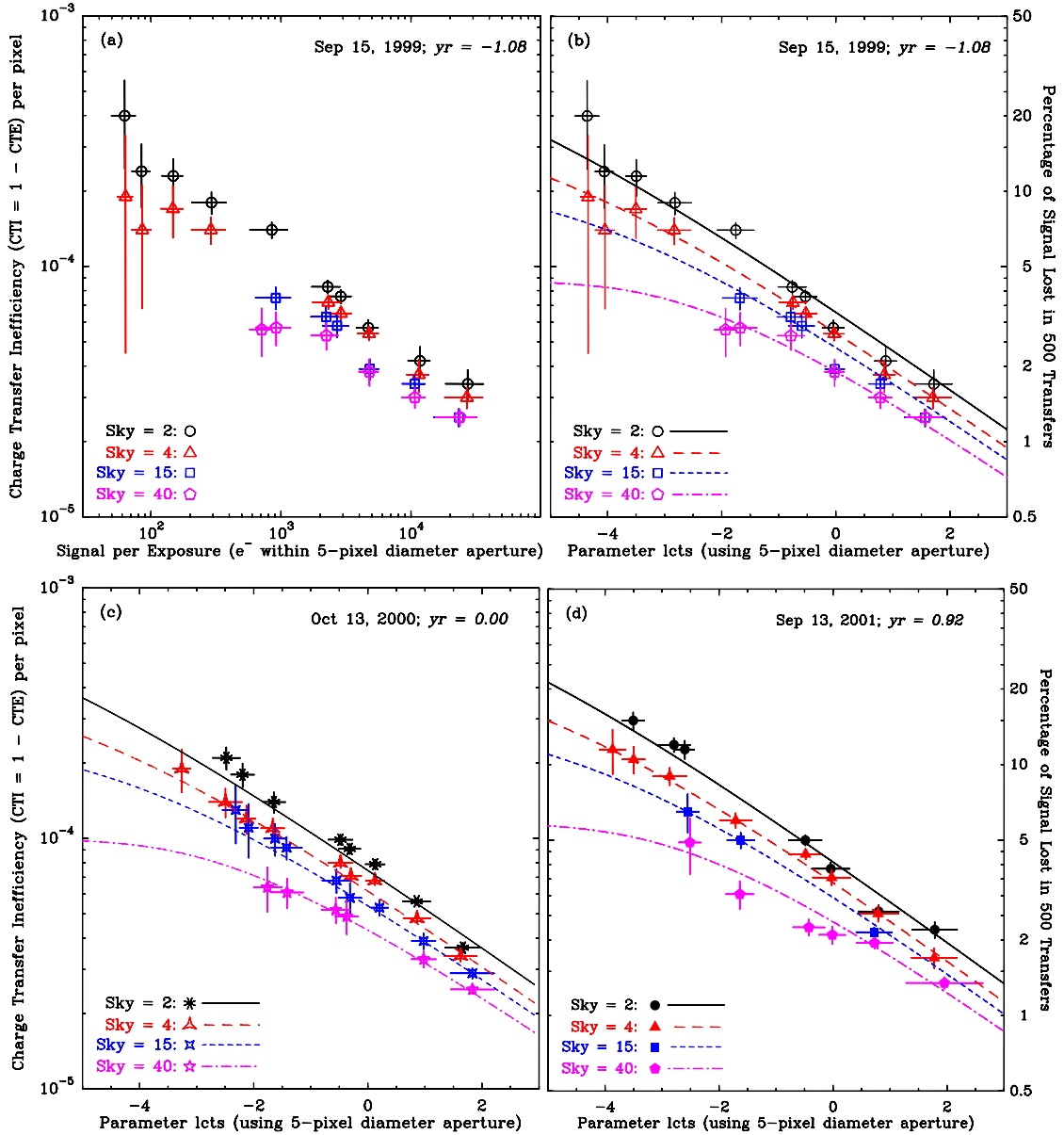


Figure 7. Panel (a): CTI vs. object signal for the September 1999 dataset. Panels (b)–(d): CTI vs. parameter “lcts” (see eq. 1), separately for each observation epoch (1999 through 2001). The percentage charge loss at row 500 of the CCD is shown on the right side of panels (b) and (d). The lines in panels (b)–(d) depict the best-fit CTI parametrization as discussed in Section 3.1. Symbols and line types are associated with specific sky background levels, as depicted in the legend of each panel. The CTI parametrization fits the data to within 7% (max. error), leading to a photometric accuracy of $\lesssim 1\%$ after applying the correction.

3.2. Applying the CTI Correction Formula

Once the CTI has been determined for a given object by applying Eq. (1) using the coefficients in Table 1, the actual CTI correction to the observed counts is:

$$\text{Corrected Counts} = \frac{\text{Observed Counts}}{1 - \text{CTI} \times \left(\frac{1024}{\text{YBIN}} - \text{YCEN} \right)}$$

where YBIN is the binning factor in the Y direction (data header keyword BINAXIS2) and YCEN is the observed Y coordinate of the object in question.

4. Concluding Remarks

We have reviewed the methods used to monitor the evolution of the CTI of the STIS CCD, using both internal and external exposures which provide measures that are directly applicable to typical imaging and spectroscopic observations with the STIS CCD. We analyzed the imaging datasets observed through the fall of 2001 to derive a functional form for the CTI correction in a semi-empirical fashion. After applying this CTI correction formula to observed data, systematic residuals stay within 1%.

In the near future, we will perform a similar characterization of the CTE loss occurring for *spectroscopic* observations of point sources. CTE correction formulae for STIS CCD observations will be incorporated in a STSDAS task within the STIS package. In case of imaging photometry, we will provide an option to use either ASCII or STSDAS tables (e.g., those supplied by the DAOPHOT package) as input files to the task.

As always, STIS observers will be informed of STIS calibration updates by email, through the *Space Telescope Analysis Newsletter* which is also available through the “Document Archive” section of the STIS website at <http://www.stsci.edu/hst/stis>.

Acknowledgments. We appreciated discussions with Ron Gilliland, Adam Riess, and Brad Whitmore.

References

- Dolphin, A. E. 2000, *PASP*, 112, 1397
- Gilliland, R. L., Goudfrooij, P., & Kimble, R. A. 1999, *PASP*, 111, 1009
- Goudfrooij, P., Kimble, R. A., Gilliland, R. L., & Potter, M. 2003, in preparation
- Janesick, J., Soli, G., Elliot, T., & Collins, S., 1991 SPIE Electronic Imaging and Technology Conference on *Solid State Optical Sensors II*, 1147
- Kimble, R. A., Brown, L., Fowler, W. B., Woodgate, B. E., Yagelowich, J. J., et al. 1994, *Proc. SPIE*, 2282, p. 169
- Kimble, R. A., Goudfrooij, P., & Gilliland, R. L., 2000, *Proc. SPIE*, 4013, p. 532
- Leitherer, C. & Bohlin, R. C. 1999, *Instrument Science Report STIS 97-13* (Baltimore: STScI), available through <http://www.stsci.edu/hst/stis>
- Press, W. H., Flannery, B. P., Teukolsky, S. A., & Vetterling, W. T. 1992, *Numerical Recipes in Fortran* (Cambridge: Cambridge University Press)
- Riess, A., Biretta, J., & Casertano, S. 1999, *Instrument Science Report WFPC2 99-04* (Baltimore: STScI), available through <http://www.stsci.edu/instruments/wfpc2>
- Stetson, P. B. 1987, *PASP*, 99, 191
- Whitmore, B. C., Heyer, I., & Casertano, S. 1999, *PASP*, 111, 1559
- Woodgate, B. E., Kimble, R. A., Bowers, C. W., Kraemer, S., Kaiser, M. E., et al. 1998, *PASP*, 110, 1183